

CONSTRAINTS ON THE RADIAL VARIATION OF GRAIN GROWTH IN THE AS 209 CIRCUMSTELLAR DISK

LAURA M. PÉREZ¹, JOHN M. CARPENTER¹, CLAIRE J. CHANDLER², ANDREA ISELLA¹, SEAN M. ANDREWS³, LUCA RICCI¹,
NURIA CALVET⁴, STUARTT A. CORDER⁵, ADAM T. DELLER⁶, CORNELIS P. DULLEMOND⁷, JANE S. GREAVES⁸, ROBERT J.
HARRIS³, THOMAS HENNING⁹, WOJIN KWON¹⁰, JOSEPH LAZIO¹¹, HENDRIK LINZ⁷, LEE G. MUNDY¹², ANNEILA I.
SARGENT¹, SHAYE STORM¹², LEONARDO TESTI^{13,14}, DAVID J. WILNER³

Draft version July 23, 2018

ABSTRACT

We present dust continuum observations of the protoplanetary disk surrounding the pre-main sequence star AS 209, spanning more than an order of magnitude in wavelength from 0.88 to 9.8 mm. The disk was observed with sub-arcsecond angular resolution ($0.2'' - 0.5''$) to investigate radial variations in its dust properties. At longer wavelengths, the disk emission structure is notably more compact, providing model-independent evidence for changes in the grain properties across the disk. We find that physical models which reproduce the disk emission require a radial dependence of the dust opacity κ_ν . Assuming that the observed wavelength-dependent structure can be attributed to radial variations in the dust opacity spectral index (β), we find that $\beta(R)$ increases from $\beta < 0.5$ at ~ 20 AU to $\beta > 1.5$ for $R \gtrsim 80$ AU, inconsistent with a constant value of β across the disk (at the 10σ level). Furthermore, if radial variations of κ_ν are caused by particle growth, we find that the maximum size of the particle-size distribution (a_{max}) increases from sub-millimeter-sized grains in the outer disk ($R \gtrsim 70$ AU) to millimeter and centimeter-sized grains in the inner disk regions ($R \lesssim 70$ AU). We compare our observational constraint on $a_{max}(R)$ with predictions from physical models of dust evolution in proto-planetary disks. For the dust composition and particle-size distribution investigated here, our observational constraints on $a_{max}(R)$ are consistent with models where the maximum grain size is limited by radial drift.

Subject headings: protoplanetary disks — stars: individual (AS 209)

1. INTRODUCTION

The growth of sub-micron-sized dust grains into millimeter and centimeter-sized particles is a fundamental component of the planet formation process (Beckwith et al. 2000; Natta et al. 2007). Grain growth directly affects the optical properties of dust particles (Henning & Stognienko 1996; D’Alessio et al. 2001), with composition and temperature having a lesser impact (Henning & Mutschke 1997; Semenov et al. 2003;

Boudet et al. 2005). At long wavelengths, the slope α of the spectral energy distribution (SED, $\nu S_\nu \propto \nu^{\alpha+1}$) can be related to the spectral index of the dust opacity β ($\kappa_\nu \propto \nu^\beta$), in particular $\beta = \alpha - 2$ for optically thin warm dust (Beckwith & Sargent 1991; Miyake & Nakagawa 1993). The millimeter dust opacity slope for small interstellar medium (ISM) dust grains is $\beta_{\text{ISM}} \sim 1.7$ (Li & Draine 2001). A smaller value of β is measured if larger millimeter-sized grains are present (D’Alessio et al. 2001; Draine 2006).

Observations of dust in disks from sub-mm to cm wavelengths (Testi et al. 2001; Calvet et al. 2002; Testi et al. 2003; Natta & Testi 2004; Wilner et al. 2005; Rodmann et al. 2006; Lommen et al. 2009; Ricci et al. 2010a,b) have provided strong evidence for grain growth in disks. These results, obtained mainly from spatially unresolved observations, assumed a constant dust opacity (i.e. constant β) throughout the disk. However, theoretical models of dust transport, fragmentation, and size evolution in proto-planetary disks predict that the average size of grains varies with the distance to the central star (hereafter referred to as radius, Dullemond & Dominik 2005; Birnstiel et al. 2010). Hence, radial variations in the dust opacity slope are expected.

The increased sensitivity and angular resolution of current interferometers has enabled the first studies of radial variations of grain growth within circumstellar disks. Observations of disks in Taurus at 1.3 and 3 mm with CARMA¹⁵ (Isella et al. 2010) and PdBI¹⁶

¹ California Institute of Technology, 1200 East California Blvd, Pasadena, CA 91125, USA

² National Radio Astronomy Observatory, P.O. Box O, Socorro NM 87801, USA

³ Harvard-Smithsonian Center for Astrophysics, 60 Garden Street, Cambridge, MA 02138, USA

⁴ University of Michigan, 830 Dennison Building, 500 Church Street, Ann Arbor, MI 48109, USA

⁵ Joint ALMA Observatory, Av. Alonso de Córdova 3107, Vitacura, Santiago, Chile

⁶ The Netherlands Institute for Radio Astronomy (ASTRON), 7990-AA Dwingeloo, The Netherlands

⁷ Heidelberg University, Center for Astronomy, Albert Ueberle Str 2, Heidelberg, Germany

⁸ University of St. Andrews, Physics and Astronomy, North Haugh, St Andrews KY16 9SS

⁹ Max-Planck-Institut für Astronomie, Königstuhl 17, 69117 Heidelberg, Germany

¹⁰ University of Illinois, 1002 West Green St., Urbana, IL 61801, USA

¹¹ Jet Propulsion Laboratory, California Institute of Technology, 4800 Oak Grove Dr, Pasadena, CA 91106

¹² University of Maryland, College Park, MD 20742, USA

¹³ European Southern Observatory, Karl Schwarzschild str. 2, 85748 Garching, Germany

¹⁴ INAF-Osservatorio Astrofisico di Arcetri, Largo E. Fermi 5, 50125 Firenze, Italy

¹⁵ Combined Array for Research in Millimeter-wave Astronomy

(Guilloteau et al. 2011), have constrained β as a function of radius. However, these results are only sensitive to radial variations larger than $\Delta\beta \sim 0.6 - 0.7$ at 3σ in the best cases, limited by the small wavelength separation between the two bands being observed. Increased wavelength coverage has been obtained by adding cm-wave observations (Banzatti et al. 2011), but the low signal-to-noise ratio, before the Karl G. Jansky Very Large Array (VLA) upgrade, made such studies challenging. To significantly improve these constraints, and effectively compare them to theoretical predictions of grain growth, increased wavelength coverage and enhanced sensitivity are required.

This letter presents the first results of a program that combines spatially resolved observations from submillimeter to centimeter wavelengths, to constrain radial variations of grain growth within circumstellar disks. The pre-main sequence star AS 209, also known as V1121 Oph, is a classical K5 T-Tauri star with high accretion rate ($1.3 \times 10^{-7} M_{\odot} \text{ yr}^{-1}$, Johns-Krull et al. 2000). AS 209 is isolated from the main ρ -Ophiuchus cloud ($\alpha = 16^{\text{h}}49^{\text{m}}15.3^{\text{s}}$, $\delta = -14^{\text{d}}22^{\text{m}}08.7^{\text{s}}$) at a distance of 131 ± 50 pc (van Leeuwen 2007). Resolved 0.88 mm continuum observations reveal a smooth radial density structure down to $0.3'' \sim 40$ AU (Andrews et al. 2009, 2010). We obtained additional spatially resolved observations at $\lambda > 0.88$ mm, to study grain growth inside the AS 209 disk.

2. AS 209 OBSERVATIONS

Submillimeter Array (SMA) observations at 0.88 mm were obtained between May 2006 and June 2007, in C, E, and V configurations ($\sim 0.3''$ resolution), with total continuum bandwidth of 4 GHz. Its integrated flux density is 577 ± 60 mJy at 0.88 mm. Andrews et al. (2009) presented a detailed discussion of the observations and data reduction.

CARMA observations at 2.8 mm were obtained between December 2009 and March 2010, in C, B, and A configurations spanning baselines of 30-1800 m ($\sim 0.5''$ resolution), with total continuum bandwidth of 8 GHz. Its integrated flux density is 40 ± 6 mJy at 2.8 mm. Atmospheric conditions were good, with zenith opacities $\tau_{230 \text{ GHz}} \leq 0.15$, except for B configuration observations where $\tau_{230 \text{ GHz}} \sim 0.4$. Data were calibrated using the Multichannel Image Reconstruction, Image Analysis and Display (MIRIAD) software package (Sault et al. 1995).

VLA observations at 8.0 and 9.8 mm (Ka-band) were obtained between Jan-May 2011 (project AC982), in CnB and BnA configurations, spanning baselines of 350 m to 36.4 km ($\sim 0.2''$ resolution). Two 1 GHz basebands centered at 30.5 and 37.5 GHz provided 2 GHz of continuum bandwidth. At 8.0 and 9.8 mm the integrated flux density of AS 209 is 1.2 ± 0.1 and 0.7 ± 0.1 mJy respectively. Data were calibrated using the Common Astronomy Software Applications (CASA).

For all datasets, quasar observations interspersed between science target observations were used to calibrate the complex antenna gains. Absolute flux calibration was obtained by observing Neptune for CARMA, Uranus and Titan for SMA, and 3C286 for VLA. For each telescope, calibrated visibilities coming from different configurations

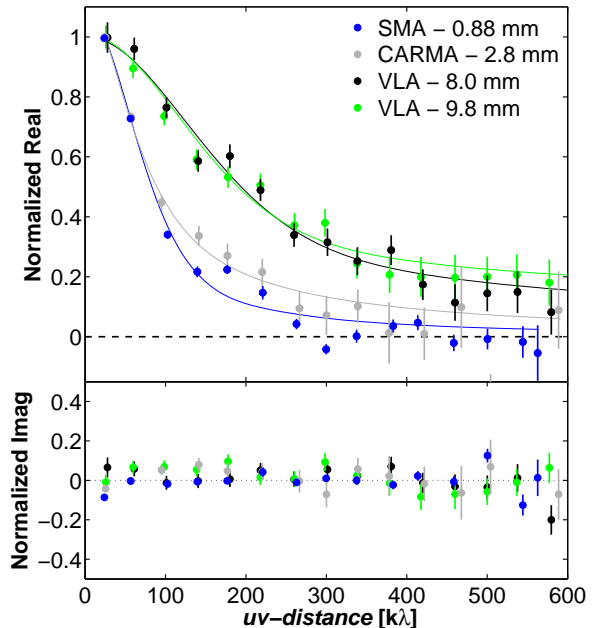


FIG. 1.— Real and imaginary part of the bin-averaged visibilities from AS 209 as a function of spatial frequency (uv -distance). Disk visibilities have been normalized by the measured flux density between uv -distances of 0–40 [$k\lambda$], and deprojected assuming $PA = 86^\circ$, $i = 38^\circ$ (Andrews et al. 2009). Filled circles and errorbars: correlated emission observed at different wavelengths, continuous lines: best-fit at each wavelength.

urations were corrected for proper motion (van Leeuwen 2007) and compared over the spatial frequencies where these configurations overlap; these were found to agree within the absolute flux scale uncertainty ($\sim 10 - 15\%$). Fourier inversion of the visibilities and cleaning of the dirty image to produce dust emission map, were performed using CASA.

3. OBSERVATIONAL RESULTS

Figure 1 presents the normalized Real/Imaginary part of the correlated emission from AS 209 as a function of spatial frequency (uv -distance), for each wavelength. The real part of the visibility will be constant with increasing spatial frequency for an unresolved point-source. In contrast, for AS 209 we measure a declining profile with increasing uv -distance, indicative of spatially resolved emission at all wavelengths. Furthermore, short-wavelength emission (0.88, 2.8 mm) diminishes faster than long-wavelength emission (8.0, 9.8 mm); therefore, the structure at long-wavelengths is more compact than at short-wavelengths.

Before interpreting these observational results in terms of grain properties variations, we explore other explanations for the differing amplitude profiles: (1) seeing affecting high frequency observations would have to be $> 1.2''$ at 0.88 mm ($\times 10$ larger than observed seeing; Andrews et al. 2009), (2) optically thick emission at short wavelengths: modeling of these observations (§4) indicates $\tau < 1$ over the scales studied. Consequently, we conclude that the long-wavelength emission comes from a smaller region than the short-wavelength emission.

Before proceeding, we account for continuum emission not arising from dust, such as free-free emission

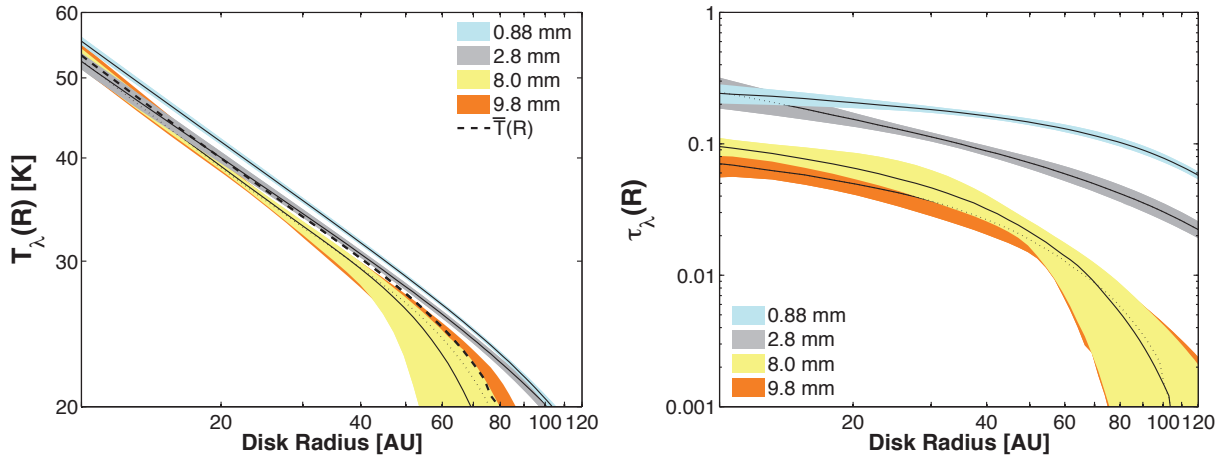


FIG. 2.— *Left:* $T_\lambda(R)$ inferred from separate modeling of our multi-wavelength observations, assuming a constant dust opacity with radius. *Right:* Optical depth $\tau_\lambda(R) = \kappa_\lambda \times \Sigma_\lambda(R)$ inferred from separate modeling of multi-wavelength observations, assuming a radially constant κ_λ . Colored regions: 3σ confidence interval constrained by our observations, continuous line: best-fit model, dashed line on left panel: average temperature profile. The different $\Sigma(R)$ and $T(R)$ profiles for each wavelength portray a varying dust opacity with radius, and because of this, none of them is the true surface density and temperature profile of the disk.

from photo-evaporative stellar winds. Such emission originates near the star (within 10 AU for TW Hya, Pascucci et al. 2011), appearing as a point-source at the resolution of our observations. Indeed, in addition to the resolved emission detected with VLA, we detect a point-like component (at uv -distances > 900 k λ) with a flux density of 0.08 ± 0.02 mJy (8 mm) and 0.10 ± 0.02 mJy (9.8 mm), corresponding to $\sim 7\%$ and $\sim 14\%$ of the total emission at these wavelengths. However, VLA observations at 5.2 cm from the Disks@EVLA collaboration¹⁷ (Chandler et al. in prep) place a 3σ upper limit of $72 \mu\text{Jy}$, suggesting that the point-like emission at 8 and 9.8 mm may be dust emission. Nonetheless, we conservatively include this point-like emission as a free-free component in models described next.

4. MODELING RESULTS

Observations were analyzed using the disk emission model described in Isella et al. (2009). The disk structure follows the two-layer disk approximation (Chiang & Goldreich 1997), defined by the boundary between the disk surface layer (optically thin to stellar radiation) and the disk interior (optically thick to stellar emission). The disk is passively heated by AS 209 ($L_\star = 1.5 L_\odot$, $T_\star = 4250$ K, $M_\star = 0.9 M_\odot$, Andrews et al. 2009). Dust in the disk surface absorbs the stellar radiation and re-radiates this energy at longer wavelengths. Because this hot dust layer will be optically thin to its own thermal radiation, half of the surface layer emission will be radiated outwards while the rest will be radiated towards the disk, heating up its interior.

For the density structure, we employ the self-similar solution for a viscous accretion disk (Lynden-Bell & Pringle 1974)

$$\Sigma(R) = \Sigma_t \left(\frac{R_t}{R} \right)^\gamma \times \exp \left[-\frac{1}{2(2-\gamma)} \left[\left(\frac{R}{R_t} \right)^{(2-\gamma)} - 1 \right] \right] \quad (1)$$

¹⁷ <https://safe.nrao.edu/evla/disks/>

where Σ_t corresponds to the surface density at radius R_t . This $\Sigma(R)$ prescription behaves as a power-law for small radii, decreasing exponentially at large radii.

We compute the dust opacity κ_ν using Mie theory, assuming a population of compact spherical grains in a power-law size distribution, $n(a) \propto a^{-q}$, for $a_{min} < a < a_{max}$ with $a_{min} = 0.01 \mu\text{m}$. Optical constants for astrophysical grain components were obtained from Semenov et al. (2003), Zubko et al. (1996), and Warren (1984). Fractional abundances were adopted from Pollack et al. (1994, in volume: 8% silicates, 30% organics, 62% water ice). Recent revisions of the solar oxygen abundance (Asplund et al. 2009) would reduce the amount of water-ice. However, the effect on the disk modeling is minimal, with a difference in the disk structure constraints well within their uncertainties as shown by Isella et al. (2010).

The best-fit model to a single wavelength observation is found through χ^2 minimization with 3 free parameters that describe the surface density (Σ_t, R_t, γ), since the disk geometry is fixed based on molecular line observations ($i = 38^\circ$, PA = 86° Andrews et al. 2009). The χ^2 probability distribution is sampled by varying the free parameters, generating a model state and comparing this state to the data in Fourier space, following the Markov Chain Monte Carlo (MCMC) method described in Isella et al. (2009).

For this initial model fit, we select the maximum grain size (a_{max}) and particle-size distribution slope (q) that best fit the unresolved SED from sub-mm to cm wavelengths. For AS 209, these correspond to $q = 3.5$, $a_{max} = 1.3$ mm, resulting in $\beta = 1.0$ between 0.88 and 8.0 mm. Then, assuming a constant dust opacity throughout the disk, each wavelength is fitted separately with the aforementioned physical model. We obtain best-fit $\Sigma(R)$ and $T(R)$ profiles, that will be different for each wavelength if the assumption of a radially constant dust opacity is not valid (Isella et al. 2010).

Figure 2 shows the best-fit and 3σ constraints on $T(R)$ and the disk optical depth $\tau_\lambda(R) = \kappa_\lambda \Sigma(R)$, inferred from modeling each observation separately. As can be

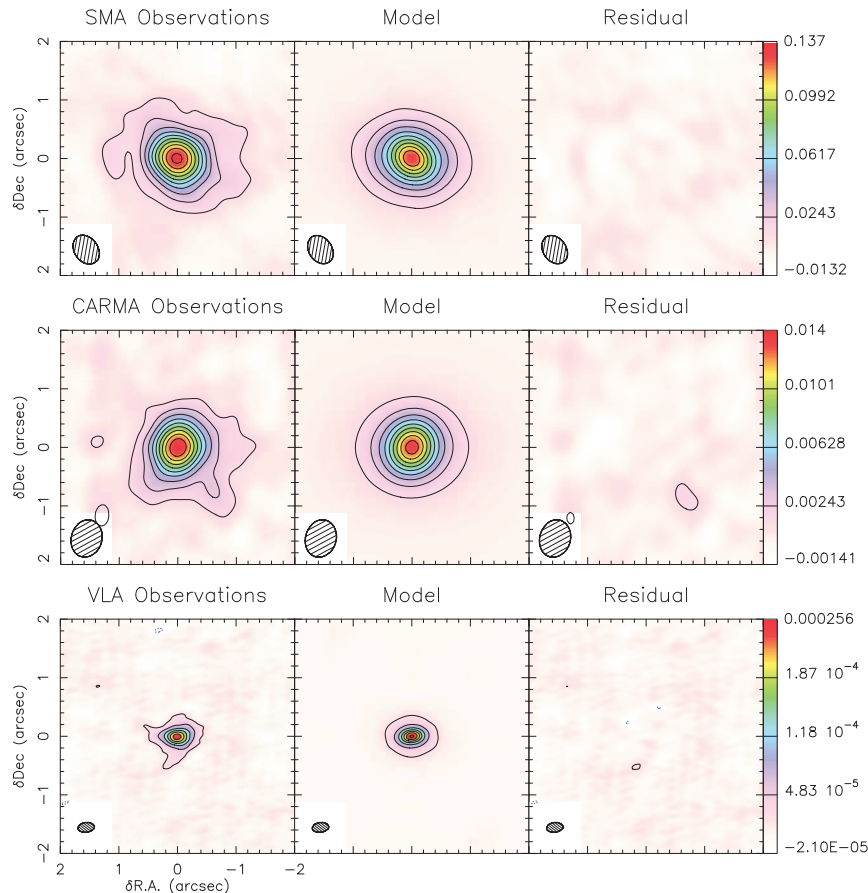


FIG. 3.— Continuum emission towards AS 209, observed at 0.88 mm (top panels), 2.8 mm (middle panels) and 8.0 and 9.8 mm (combined through multi-frequency synthesis, bottom panels). Each observation, accompanied by the best-fit disk emission and a residual map obtained by subtracting the best-fit model from the observations, used Briggs weighting with $\text{robust} = 0.7$ (SMA, CARMA), while VLA data used natural weighting. Contours start at -3σ , stepping by 3σ (CARMA, SMA) and 6σ (VLA), where σ is the RMS noise on each map: $\sigma_{\text{SMA}} = 4.4$ mJy/beam, $\sigma_{\text{CARMA}} = 0.47$ mJy/beam, $\sigma_{\text{VLA}} = 0.01$ mJy/beam.

seen in this figure, a differing $\Sigma(R)$ and $T(R)$ was inferred for each wavelength when κ_λ is assumed to be constant with radius. We constrain R_t to be large for the short-wavelength emission ($R_t = 61 \pm 2$ AU from 0.88 mm and $R_t = 60 \pm 6$ AU from 2.8 mm), compared to R_t inferred at long-wavelengths ($R_t = 24 \pm 3$ AU from 8 mm, $R_t = 26 \pm 4$ AU from 9.8 mm). We note that the derived temperature profiles differ by < 4 K for $R < 70$ AU, and by $\lesssim 10$ K for $R > 70$ AU. The best-fit model visibility profiles at each wavelength are shown as continuous lines in Figure 1. Maps of the observed emission, with corresponding best-fit model and residual emission maps are shown in Figure 3.

Since the disk is optically thin (right panel, Figure 2), the observed emission will depend directly upon the dust opacity and disk mass: $S_\lambda \propto \kappa_\lambda \times \Sigma \times B_\lambda(T)$. Hence, our observations constrain the product $\kappa_\lambda \times \Sigma \times B_\lambda(T)$, where all these physical parameters ($\kappa_\lambda, \Sigma, T$) depend on the radius, but only the dust opacity depends on the observed wavelength. The modeling presented above, assuming a constant dust opacity with radius and fitting each wavelength separately, has resulted in a wavelength-dependent $\Sigma_\lambda(R)$ and $T_\lambda(R)$, which is unphysical but telling: the assumption of a constant κ_λ with radius is likely incorrect. Radial variations of the dust opacity

are required to reconcile the differing visibility profiles (Real part vs. uv -distance, Figure 1) and the wavelength-dependent $\Sigma_\lambda(R)$ and $T_\lambda(R)$ (Figure 2).

5. DISCUSSION

5.1. Radial variations of β

Expanding on the work presented in Isella et al. (2010), if the *true* but unknown disk physical quantities are $\bar{\kappa}_\lambda(R)$, $\bar{\Sigma}(R)$, and $\bar{T}(R)$, then at each wavelength

$$\kappa_\lambda \Sigma_\lambda(R) B_\lambda(T_\lambda(R)) = \bar{\kappa}_\lambda(R) \bar{\Sigma}(R) B_\lambda(\bar{T}(R)) \quad (2)$$

where the right-hand side of this equation corresponds to the true disk properties, and the left-hand side encompasses the constraints found from our multi-wavelength observations. Taking the ratio of equation 2 for $\lambda_1 \neq \lambda_2$, and assuming that at long wavelengths $\kappa_\lambda \propto \lambda^{-\beta}$, we obtain

$$\Delta\beta(R) = \log^{-1} \left[\frac{\lambda_1}{\lambda_2} \right] \times \log \left[\frac{\Sigma_{\lambda_1} B_{\lambda_1}(T_{\lambda_1}) / B_{\lambda_1}(\bar{T})}{\Sigma_{\lambda_2} B_{\lambda_2}(T_{\lambda_2}) / B_{\lambda_2}(\bar{T})} \right] \quad (3)$$

where Σ_λ , T_λ , and \bar{T} depend on the radius R . Equation 3 is a useful prescription to constrain radial variations of the opacity spectral slope ($\Delta\beta(R) = \beta(R) - \beta_C$) in dual-wavelength observations. Here β_C corresponds to

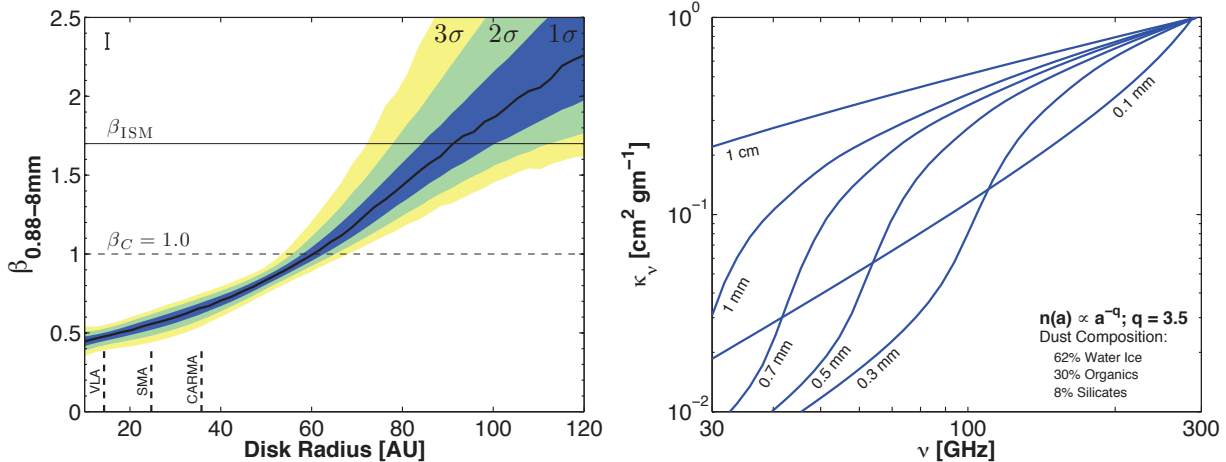


FIG. 4.— *Left*: Dust opacity spectral slope, β , vs. radius, inferred from multi-wavelength observations of the AS 209 disk. Black line: best-fit $\beta(R)$, colored areas: confidence interval constrained by our observations. Vertical dashed-lines indicate the spatial resolution of our observations, errorbar in top-left corner indicates additional systematic uncertainty on $\beta(R)$ arising from amplitude calibration uncertainty. *Right*: Dust opacity (normalized at 300 GHz) for a_{max} between 0.1-10 cm. Note that the power-law assumption, $\kappa_\nu \propto \nu^\beta$, breaks down for (sub-)mm-sized grains.

the spectral slope of the assumed radially constant dust opacity.

In the Rayleigh-Jeans regime (when $hc/\lambda \ll k_B T$, k_B : Boltzmann constant), knowledge of $\bar{T}(R)$ to derive $\Delta\beta(R)$ is unnecessary since $B_\lambda(T) \propto T$. However, in the cold outer disk and at short wavelengths, the Rayleigh-Jeans assumption is ill-founded (e.g. $h\nu \sim k_B T$ for $T = 20$ K at 0.88 mm). Consequently, we require an estimate of $\bar{T}(R)$. Since the temperature profiles inferred from each wavelength ($T_\lambda(R)$) are not very different, we average them to deduce $\bar{T}(R)$ (dashed-line on Figure 2).

Equation 3 shows that in logarithmic space $\Delta\beta(R)$ is the slope of a line that goes through points $\{x = \log(\lambda), y = \log[\Sigma_\lambda B_\lambda(T_\lambda)/B_\lambda(\bar{T})]\}$, with y evaluated at radius R . Hence, to measure $\Delta\beta(R)$ we find the slope of a straight line – in a least-square sense – that fits our constraints on the product $\Sigma_\lambda \times B_\lambda(T_\lambda)/B_\lambda(\bar{T})$ from our set of multi-wavelength observations. To set confidence intervals on $\Delta\beta(R)$, we make use of the Bayesian approach upon which our modeling is based. Since the result of the MCMC algorithm is a fully sampled posterior probability distribution function (PDF) for all the model parameters, we construct a PDF of the product $\Sigma_\lambda \times B_\lambda(T_\lambda)/B_\lambda(\bar{T})$ at each radius R and for each wavelength. Random samples of these PDFs are taken at each wavelength, the slope of the line through points $\{x = \log(\lambda), y = \log[\Sigma_\lambda \times B_\lambda(T_\lambda)/B_\lambda(\bar{T})]\}$ at a radius R , is computed. This slope corresponds to one random sampling of $\Delta\beta(R)$. Hence, the PDF for $\Delta\beta(R)$ is constructed by performing a large number of random samples. The peak of this PDF is the best-fit value of $\Delta\beta$ at radius R . Confidence intervals are derived from the region of the PDF that contains 68.3%, 95.5% and 99.7% of all samples at equal probability (1σ , 2σ , and 3σ).

Figure 4 presents the constraints on the radial variation of β obtained from our multi-wavelength observations. The values of β allowed by our observations are significantly different than $\beta_{ISM} \sim 1.7$, for $R \lesssim 70$ AU. Furthermore, we find a gradient on $\beta(R)$ inconsistent

with a constant value at the 10σ level.

5.2. Radial variations of a_{max}

To derive equation 3, the assumption of $\kappa_\lambda \propto \lambda^{-\beta}$ must be satisfied. We caution that for $a_{max} \sim 0.1$ -1 mm this approximation may break down (Draine 2006), as illustrated in Figure 4 (right). Therefore, rather than inferring $a_{max}(R)$ from $\beta(R)$, we constrain it directly by fitting a specific dust opacity $\bar{\kappa}_\lambda$ to the constraints on the product $\kappa_\lambda \times \Sigma_\lambda \times B_\lambda(T_\lambda)$ at each radius. With a knowledge of $\bar{T}(R)$, and for a fixed set of dust properties (composition and grain-size distribution), we estimate the values of a_{max} and $\bar{\Sigma}$ that satisfy equation 2, now written as

$$\kappa_\lambda \Sigma_\lambda(R) \frac{B_\lambda(T_\lambda(R))}{B_\lambda(\bar{T}(R))} = \bar{\kappa}_\lambda(a_{max}(R)) \bar{\Sigma}(R) \quad (4)$$

where the right-hand side corresponds to our model (with parameters a_{max} and $\bar{\Sigma}$), and the left-hand side has been constrained by our multi-wavelength observations (i.e. we have a PDF for the product $\kappa_\lambda \times \Sigma_\lambda(R) \times \frac{B_\lambda(T_\lambda(R))}{B_\lambda(\bar{T}(R))}$).

At each radius R , we constructed a two dimensional grid of parameters $\{a_{max}, \bar{\Sigma}\}$. At each point in the grid, we compute the product $\bar{\kappa}_\lambda(a_{max}) \times \bar{\Sigma}$ at each wavelength. We then find the probability that such measurement will have occurred (given our observational constraints on the left-hand side of equation 4), and construct the likelihood function of the parameters $\{a_{max}, \bar{\Sigma}\}$. Best-fit values for a_{max} and $\bar{\Sigma}$ are found by maximizing the likelihood, confidence intervals are obtained from the marginalized likelihoods.

Figure 5 presents our constraints on $a_{max}(R)$ and $\bar{\Sigma}(R)$ for two representative values of q . The same composition presented in §4 is assumed, however a different dust mixture will influence the derived $a_{max}(R)$. For a composition that includes updated oxygen abundances (Asplund et al. 2009), a smaller $a_{max}(R)$ is inferred ($\times 2$ smaller), well within the uncertainties of this derivation

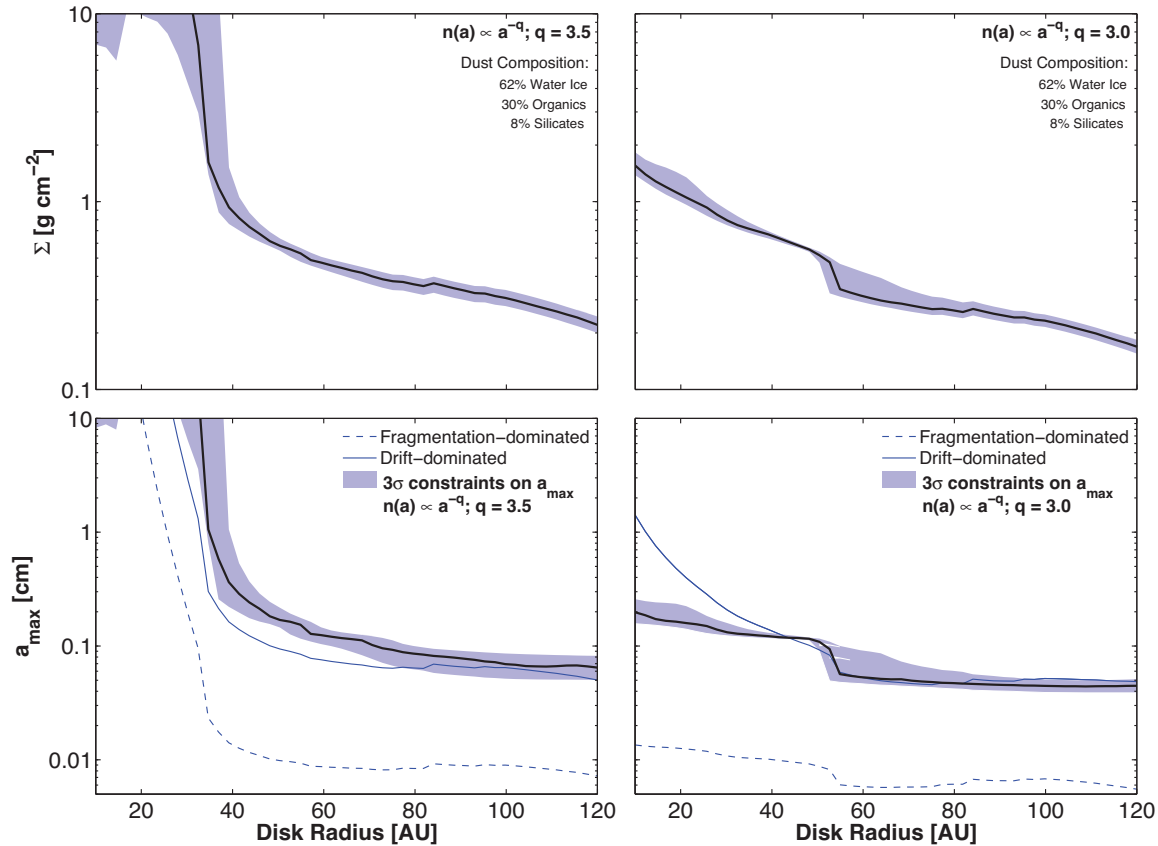


FIG. 5.— Surface density (top) and maximum grain size as a function of radius (bottom), for two grain size distributions: $q = 3.5$ (left), $q = 3.0$ (right). Black line: best-fit, shaded region: 3σ confidence interval. Assumed grain properties are specified in figure legend. We compare our observational constraints with theoretical grain evolution models (Birnstiel et al. 2012), that include fragmentation and radial drift.

given other unknown parameters (e.g. particle-size distribution slope). Across the disk, grains have grown at least up to ~ 0.5 mm, with small grains present in the outer disk and large grains in the inner disk.

We compare our observational constraints with theoretical models of grain growth, employing the approximations presented in Birnstiel et al. (2012) for the evolution of a_{max} with radius. Since the true $\bar{\Sigma}(R)$ profile constrained by our observations depends on the assumed value of q (see Figure 5), these theoretical prescriptions will depend on q as well. Our observational constraints on a_{max} are consistent with a *radial drift limited* grain population, where the head-wind felt by dust particles makes them spiral towards the star. A *fragmentation dominated* population, where the turbulent relative motion of particles causes collisions that either grow or fragment these grains, seems incompatible for standard values of the turbulence parameter ($\alpha_t = 0.01$, Shakura & Sunyaev 1973), fragmentation threshold velocity ($u_t = 10$ m/s, Blum & Wurm 2008), and 100:1 gas-to-dust ratio. These curves represent barriers that prevent further size increase, hence, the smaller of the two is considered the upper-limit to growth. However, the parameters that go into deriving the fragmentation limit are very uncertain, while the physics and parameters in radial drift are better established. Either no fragmentation barrier exists (for a low-turbulence disk, $\alpha_t \lesssim 0.001$, the maximum collision speed never reaches the fragmen-

tation threshold velocity in AS 209, making fragmentation impossible) or the gas-to-dust ratio is $\sim \times 10$ larger, allowing for the fragmentation-limited barrier to be consistent with our $a_{\text{max}}(R)$ constraint. It remains to be demonstrated whether these models reproduce the observed $\beta(R)$ profile and the millimeter fluxes. Such analysis requires numerical simulations starting from the disk parameters derived here and will be discussed in a future paper.

5.3. Summary

We have obtained multi-wavelength spatially-resolved observations at 0.88, 2.8, 8.0, and 9.8 mm of the AS 209 circumstellar disk. These observations reveal a wavelength-dependent structure, explained as radial variations of the dust opacity across the disk. We find a change in $\Delta\beta > 1$ between the inner (~ 20 AU) and outer (~ 120 AU) disk, inconsistent with a constant β value. This gradient in $\beta(R)$ implies that a significant change in the dust properties as a function of radius must exist. We interpret this gradient as a decrease in the maximum grain size with radius: going from several centimeters or more in the inner disk to sub-mm-sized grains in the outer disk. When compared with theoretical models of dust size evolution (Birnstiel et al. 2012), we find that our observational constraint on $a_{\text{max}}(R)$ agrees with a radial-drift-dominated population, for reasonable values of the composition, particle-size distribution, and disk

properties.

We acknowledge T. Birnstiel for useful discussions. A.I., J.M.C., L.M.P acknowledge support from NSF award AST-1109334. The National Radio Astronomy Observatory is a facility of the National Science Foundation operated under cooperative agreement by Associated Universities, Inc. Ongoing CARMA development and operations are supported by the National Science Foundation under a cooperative agreement, and by the

CARMA partner universities. The SMA is a joint project between the Smithsonian Astrophysical Observatory and the Academia Sinica Institute of Astronomy and Astrophysics, funded by the Smithsonian Institution and Academia Sinica. Part of this research was carried out at the Jet Propulsion Laboratory, Caltech, under a contract with the National Aeronautics and Space Administration.

*Facilities:*CARMA, SMA, VLA.

REFERENCES

- Andrews, S. M., Wilner, D. J., Hughes, A. M., Qi, C., & Dullemond, C. P. 2009, *ApJ*, 700, 1502
- Andrews, S. M., Wilner, D. J., Hughes, A. M., Qi, C., & Dullemond, C. P. 2010, *ApJ*, 723, 1241
- Asplund, M., Grevesse, N., Sauval, A. J., & Scott, P. 2009, *ARA&A*, 47, 481
- Banzatti, A., Testi, L., Isella, A., et al. 2011, *A&A*, 525, A12
- Beckwith, S. V. W., & Sargent, A. I. 1991, *ApJ*, 381, 250
- Beckwith, S. V. W., Henning, T., & Nakagawa, Y. 2000, *Protostars and Planets IV*, 533
- Birnstiel, T., Dullemond, C. P., & Brauer, F. 2010, *A&A*, 513, A79
- Birnstiel, T., Klahr, H., & Ercolano, B. 2012, *A&A*, 539, A148
- Blum, J., & Wurm, G. 2008, *ARA&A*, 46, 21
- Boudet, N., Mutschke, H., Nayral, C., et al. 2005, *ApJ*, 633, 272
- Calvet, N., D'Alessio, P., Hartmann, L., et al. 2002, *ApJ*, 568, 1008
- Chiang, E. I., & Goldreich, P. 1997, *ApJ*, 490, 368
- D'Alessio, P., Calvet, N., & Hartmann, L. 2001, *ApJ*, 553, 321
- Draine, B. T. 2006, *ApJ*, 636, 1114
- Dullemond, C. P., & Dominik, C. 2005, *A&A*, 434, 971
- Guilloteau, S., Dutrey, A., Piétu, V., & Boehler, Y. 2011, *A&A*, 529, A105
- Henning, T., & Mutschke, H. 1997, *A&A*, 327, 743
- Henning, T., & Stognienko, R. 1996, *A&A*, 311, 291
- Isella, A., Carpenter, J. M., & Sargent, A. I. 2009, *ApJ*, 701, 260
- Isella, A., Carpenter, J. M., & Sargent, A. I. 2010, *ApJ*, 714, 1746
- Johns-Krull, C. M., Valenti, J. A., & Linsky, J. L. 2000, *ApJ*, 539, 815
- Li, A., & Draine, B. T. 2001, *ApJ*, 554, 778
- Lommen, D., Maddison, S. T., Wright, C. M., et al. 2009, *A&A*, 495, 869
- Lynden-Bell, D., & Pringle, J. E. 1974, *MNRAS*, 168, 603
- Miyake, K., & Nakagawa, Y. 1993, *Icarus*, 106, 20
- Natta, A., & Testi, L. 2004, *Star Formation in the Interstellar Medium: In Honor of David Hollenbach*, 323, 279
- Natta, A., Testi, L., Calvet, N., et al. 2007, *Protostars and Planets V*, 767
- Pascucci, I., Sterzik, M., Alexander, R. D., et al. 2011, *ApJ*, 736, 13
- Pollack, J. B., Hollenbach, D., Beckwith, S., et al. 1994, *ApJ*, 421, 615
- Ricci, L., Testi, L., Natta, A., & Brooks, K. J. 2010, *A&A*, 521, A66
- Ricci, L., Testi, L., Natta, A., et al. 2010, *A&A*, 512, A15
- Rodmann, J., Henning, T., Chandler, C. J., Mundy, L. G., & Wilner, D. J. 2006, *A&A*, 446, 211
- Sault, R. J., Teuben, P. J., & Wright, M. C. H. 1995, *Astronomical Data Analysis Software and Systems IV*, 77, 433
- Semenov, D., Henning, T., Helling, C., Ilgner, M., & Sedlmayr, E. 2003, *A&A*, 410, 611
- Shakura, N. I., & Sunyaev, R. A. 1973, *A&A*, 24, 337
- Testi, L., Natta, A., Shepherd, D. S., & Wilner, D. J. 2001, *ApJ*, 554, 1087
- Testi, L., Natta, A., Shepherd, D. S., & Wilner, D. J. 2003, *A&A*, 403, 323
- van Leeuwen, F. 2007, *A&A*, 474, 653
- Warren, S. G. 1984, *Appl. Opt.*, 23, 1206
- Wilner, D. J., D'Alessio, P., Calvet, N., Claussen, M. J., & Hartmann, L. 2005, *ApJ*, 626, L109
- Zubko, V. G., Mennella, V., Colangeli, L., & Bussoletti, E. 1996, *MNRAS*, 282, 1321